Received: 17 December 2022 | Revised: 7 June 2023 | Accepted: 8 June 2023

DOI: 10.1111/jace.19291

Journal of the American Ceramic Society

RESEARCH ARTICLE

Dislocation-tuned electrical conductivity in solid electrolytes (9YSZ): A micro-mechanical approach

Qaisar Khushi Muhammad[1] | **Marcela Valderrama**[1] | **Mengkun Yue**[2,3] | **Alexander Karl Opitz**[4] | **Stefanie Taibl**[4] | **Matthäus Siebenhofer**[4] | **Enrico Bruder**[5] | **Jürgen Fleig**[4] | **Xufei Fang**[1] | **Till Frömling**[1]

[1]Division of Nonmetallic-Inorganic Materials, Department of Materials and Earth Sciences, Technical University of Darmstadt, Darmstadt, Germany

[2]AML, Department of Engineering Mechanics, Tsinghua University, Beijing, P. R. China

[3]Center for Flexible Electronics Technology, Tsinghua University, Beijing, P. R. China

[4]Christian-Doppler-Laboratory for Ferroic Materials, Institute of Chemical Technologies and Analytics, Vienna University of Technology, Vienna, Austria

[5]Division of Physical Metallurgy, Department of Materials and Earth Sciences, Technical University of Darmstadt, Darmstadt, Germany

Correspondence
Qaisar Khushi Muhammad and Till Frömling, Division of Nonmetallic-Inorganic Materials, Department of Materials and Earth Sciences, Technical University of Darmstadt, Alarich-Weiss-Str. 2, Darmstadt 64287, Germany.
Email: muhammad@ceramics.tu-darmstadt.de and Froemling@ceramics.tu-darmstadt.de

Funding information
Austrian Research Promotion Agency (FFG), Grant/Award Number: 865864; Austrian Science Fund (FWF), Grant/Award Number: P31654-N37; Projekt DEAL; Deutscher Akademischer Austauschdienst, Grant/Award Number: 91669061; Athene Young Investigator Program: Technical University of Darmstadt

Abstract

Tailoring the electrical conductivity of functional ceramics by introducing dislocations is a comparatively recent research focus, and its merits were demonstrated through mechanical means. Especially bulk deformation at high temperatures is suggested to be a promising method to introduce a high dislocation density. So far, however, controlling dislocation generation and their annihilation remains difficult. Although deforming ceramics generate dislocations on multiple length scales, dislocation annihilation at the same time appears to be the bottleneck to use the full potential of dislocations-tailoring the electrical conductivity. Here, we demonstrate the control over these aspects using a micromechanical approach on yttria-stabilized zirconia - YSZ. Targeted indentation well below the dislocation annihilation temperature resulted in extremely dense dislocation networks, visualized by chemical etching and electron channeling contrast imaging. Microcontact-impedance measurements helped evaluate the electrical response of operating individual slip systems. A significant conductivity enhancement is revealed in dislocation-rich regions compared to pristine ones in fully stabilized YSZ. This enhancement is mainly attributed to oxygen ionic conductivity. Thus, the possibility of increasing the conductivity is illustrated and provides a prospect to transfer the merits of dislocation-tuned electrical conductivity to solid oxygen electrolytes.

KEYWORDS
dislocations, mechanical deformation, nanoindentation, oxygen–ionic conductivity, SOEC, SOFC, solid electrolytes, yttria-stabilized zirconia

1 | INTRODUCTION

Dislocations (one-dimensional defects) are classically known for their key role in the mechanical properties of metals.[1,2] The dislocation motion in a slip system, occurring at first on a micro and then macro level through the crystal, stimulates the plastic deformation.[3,4] Nevertheless, in the case of ceramics, dislocation motion is rather restricted due to the limited slip systems. Furthermore, high-temperature sintering of ceramic materials usually leads to the annihilation of dislocations existing within the raw powder. Collectively, this renders dislocations often irrelevant to the mechanical properties of ceramics.[5,6] However, it was demonstrated decades ago that many ceramics, particularly single crystals, can be plastically deformed due to dislocation introduction and their movement.[7–10] Some ceramic single crystals, for example, CaF_2,[11,12] MgO,[13,14] and LiF,[15–17] are deformable at room temperature,[18] whereas others show plasticity only at elevated temperatures.[19] It was the knowledge of dislocation mechanics that brought ceramic plastic deformation into vogue for a long time, mostly dealing with the influence of dislocations on ceramic mechanical properties.[20–26]

Recently, doping-like properties have been achieved in functional ceramics by inducing dislocations as an alternative to point defects.[27–29] It was illustrated that the control of the mesoscopic structure of dislocations is the key to tuning the functional properties, for example, electrical conductivity.[28,29] These reports address the complex set of influencing factors in terms of mesoscopic dislocation structure, their arrangement, core structure, and surrounding space charge.[28,30] Especially for rutile (TiO_2), it was established that engineering the inter-dislocation spacing may induce several orders of magnitude higher electrical conductivity on a local scale.[28,29] This indicates the potential of dislocations in tuning the electrical conductivity beyond the solubility limits of chemical doping and encourages applying this strategy to other material systems.

Yttria-stabilized zirconia (ZrO_2 doped with Y_2O_3; YSZ) is an excellent oxygen-conducting ceramic material[31,32] and acts as a model material representing fast oxide ion conductors. Its application in solid oxide fuel/electrolysis cells (SOFC/SOECs) and oxygen sensors gives YSZ technological importance.[33] However, modern and efficient SOFCs demand a reduction in their current operating temperatures (<800°C). To achieve this, research is invested in designing an electrolyte material system that is more or equally conductive at a lower temperature (<800°C).[34] To this end, the electrical conductivity of YSZ is mostly modified by point defect engineering.[35–38] Nevertheless, conventional doping strategies suffer from poor solubility limits or vacancy–dopant interactions, decreasing oxygen diffusion.[39–41] Therefore, no conductivity enhancement can be obtained above ca. 8–9 mol% yttria doping in ZrO_2.[33,42,43] However, considering the early developments, tuning the electrical properties of YSZ by mechanically induced dislocations could be an option.[44,45]

So far, the detailed knowledge was mostly limited to theoretical studies postulating that the strain field around dislocations might weaken the local oxygen–cation (O^{2-}–Zr^{4+}, Y^{3+}) bonds, resulting in an increase in the migration space for oxygen vacancies and thus contributing to the decreased charge diffusion barrier.[46–49] A previously determined minor increase in electrical conductivity (~10%) due to dislocations also hints toward higher ionic conductivity; nevertheless, the difference in electrical transport was not extensive.[44,45] Based on transmission electron microscopy results and additional computational evaluations, it was rationalized that the strain field surrounding the dislocations in YSZ should be high enough to generate high oxygen conductivity.[46,48,49] Nevertheless, convincing experimental proof has been provided only recently.[50] It was shown that an extremely dense mesoscopic dislocation structure could be induced by utilizing a notch in YSZ. The stress concentration around the notch helped generate a dislocation density of ca. 9×10^{13} m^{-2} on a local scale.[50] Targeted electrical investigations on these regions (with high dislocation density) revealed an increase in electrical transport by a factor of three compared to undeformed (pristine) areas.[50] Time-of-flight secondary ion mass spectrometry provided further evidence that oxygen–ion transport was responsible for the change in conductivity in the specimens containing a high density of dislocations.[50] Even though no transport coefficients (oxygen diffusion or incorporation coefficients) were evaluated, it was illustrated that the oxygen transport in dislocation regions is high.

Generating dislocations in YSZ typically consider the high-temperature bulk deformation method, as thermal

activation of dislocation mobility favors plasticity at elevated temperatures.[20–23] This technique probes the large bulk volume by activating a favorable slip system and generates dislocation networks. However, bulk deformation method limitations arise from the process control itself, that is, with this method, although reasonably high plastic strains could be achieved,[51,52] yet this does not guarantee a maximum dislocation density in the deformed specimens. The fundamental reason for this is the creep-controlled deformation mechanism.[53] During deformation, dislocations are generated and multiplied; however, dislocations start to annihilate at some point until their generation, and annihilation rates become the same.[5,53] This situation worsens, particularly at higher deformation temperatures,[53] when a seemingly deformed specimen (with an apparent large plastic strain) may have already lost a substantial fraction of dislocation density. Thus, the plastic deformation is carried by the instantaneously available dislocation density.[5,53] This calls for an alternative approach, limiting the dislocation annihilation or deforming YSZ at relatively-low temperatures in the first place.

The indentation technique with its nano/micro-mechanical variants is becoming much more applicable and feasible due to its compatibility with many functional devices and materials.[54,55] This method possesses great potential for probing small volumes yet providing dense dislocation networks, as also exemplified for YSZ.[56–58] Targeted indentation is achievable not only at room temperature [56] but can also be expanded to high temperatures.[59] Moreover, customized loading and control over the (center-to-center) indentation spacing make this technique even more powerful in generating localized and dense dislocation networks.[56]

This study employs a micro-mechanical (indentation) approach to induce dislocation networks in YSZ at drastically lower temperatures (i.e., room temperature and 600°C) than those needed for bulk deformation (e.g., at 1400°C).[50] Controlled indentation conditions are optimized to activate multiple slip systems.[56] Large plastic zones expanding to different lengths with extremely dense mesoscopic dislocation density are obtained far beyond the ones achieved by bulk deformation at relatively high temperatures. Through this approach, we further investigate the electrical response of indentation-induced dislocations by probing individual slip systems with the help of targeted microcontact-impedance spectroscopy.[60] This way, an alternative method is explored to avoid creep-controlled dislocation annihilation, so far acting as a bottleneck in accessing the full potential of dislocation-tuned electrical conductivity.

2 | EXPERIMENTAL PROCEDURES

2.1 | Sample preparation

Skull melt grown ~9 mol% Y_2O_3–ZrO_2 (9YSZ) single crystals with the geometry of 4 × 4 × 8 mm^3 were purchased from MaTeck Material-Technologie & Kristalle GmbH, Jülich, Germany. The original orientation of the crystals was (110) (011) and *c*-(100); however, due to their optimal etchability,[56] {111} planes were extracted (Wire Saw Solutions Group LLC, PA, USA), followed by sequential polishing (Phoenix 4000, Jean Wirtz GmbH, Düsseldorf, Germany) and fine Vibro-polishing (OP-S from Struers, Copenhagen, Denmark) to achieve scratch-free surfaces. This way, dislocations could be visualized by the facile chemical etching technique (details in the following section). The final orientation of the single crystal specimens was (111), (1 $\bar{1}$ 0), and (11 $\bar{2}$) (Figure 1A). The symmetry of the planes was further verified with Laue Back-Reflection analysis (Figure S1).[61] It has to be noted that the top images in Figure 1 are from laser microscopy investigations and are thus treated as measurement data embedded in a larger schematic.

2.2 | Room-temperature (Vickers) indentation and subsequent polishing

Room-temperature Vickers-indentation tests were performed on non-etched (111) planes of YSZ single crystals with an optimized load of 0.1 N and a dwell time of 10 s to mark an array of 5 × 5 indents with a center-to-center spacing of 5 μm. During these tests, the diagonal of the indenter was kept parallel to the [11 $\bar{2}$] direction (Figure 1A,B, and Figure S2A). To remove the indentation damage, specimens were mechanically polished (Phoenix 4000, Jean Wirtz GmbH, Düsseldorf, Germany) using 0.06 μm colloidal silica (MasterMet 2, Buehler, Illinois, USA) with a rotational speed of 150 rev. min^{-1} at a pressure of 1.6 bar. Later, Vibro-polishing (Jean-Wirtz GmbH, Düsseldorf, Germany) was done in a 40 mL solution of water and 0.04 μm colloidal silica (OP-S from Struers, Copenhagen, Denmark) with an optimized ratio of 8:1. This step was performed to remove any stresses or dislocations related to polishing before further analysis (polishing depths are provided in the respective images/sections).

2.3 | High-temperature (Berkovich) indentation

Another set of 4 × 4 indents was marked with a Berkovich indenter (Hysitron TI950 TriboIndenter, Bruker,

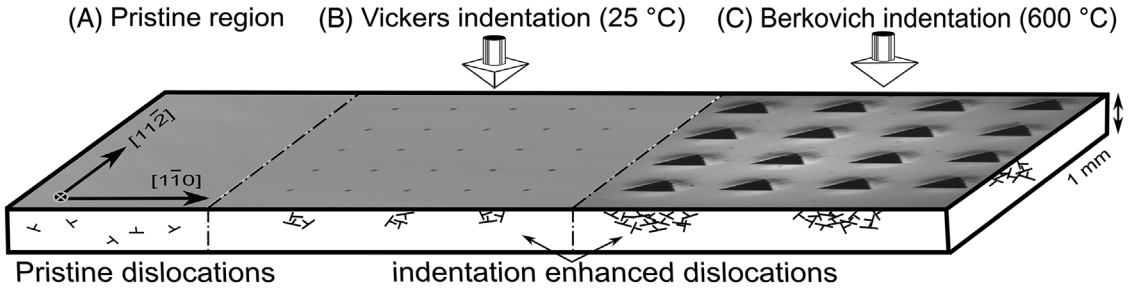

FIGURE 1 Schematic illustration of geometry and orientation of the 9YSZ specimens indented at room temperature and 600°C along with respective indenter configurations. The actual laser microscopy images for each region are provided on top of the schematic: (A) laser microscope image of a scratch-free pristine (111) plane; (B) 5 × 5 array of 0.1 N Vickers indents marked at a (center-to-center) distance of 5 μm at room temperature; (C) set of 4 × 4 Berkovich indentation imprints, center-to-center 100 μm apart, marked at 600°C. Material pile-up is visible when indentation is performed at high temperatures.

Massachusetts, US) using a 4 N load with a dwell time of 15 s, this time with a sample temperature of 600°C (Figure 1C). The indentation parameters, that is, load, substrate temperature, and spacing between the indents, were optimized for crack-free deformation before performing the final experiments. Similar to the room-temperature indentation, the Berkovich-indenter tip was also kept parallel to the [11 $\bar{2}$] direction (Figure 1C). However, the polishing time of the high-temperature indented specimens was slightly different than the ones indented at room temperature. This is because of the longer time needed to eliminate the surface pile-up and the indent imprint. Total polishing depth was measured by using a laser microscope (LEXT; OLS5000, Olympus Corporation, Japan) after a regular interval of polishing. Nevertheless, due to the high fracture toughness and low removal rate of YSZ,[5] an initial coarse polishing step was performed using 1/4 μm diamond paste (DP Paste M, Struers, Copenhagen, Denmark) coated polishing discs (MD-System, Struers, Copenhagen, Denmark) for 1 min using the same rotational speed and pressure described earlier.

2.4 | Mesoscopic dislocation density and arrangement

Chemical etching combined with laser microscopy was employed to evaluate the pristine dislocation density and image the deformation structures around the indents. For this, fine polished, pristine specimens with (111) planes were immersed in a molten KOH bath (at 500°C) for 15 min. During the etching process, dislocation lines exiting the surface were more strongly attacked than the defect-free bulk material. The dislocations are then imaged in the form of etch pits at the (111) surface, providing pristine dislocation density in these specimens (refer to Figure S4).[56] A similar etching process revealed slip traces around the post-polished indents (details in Section 3). Field emission-scanning electron microscopy (FESEM: XL30FEG, Philips, Amsterdam, the Netherlands) was used to image the small-spaced slip traces and dislocation arrangements (Figure 2). Atomic force microscopy was employed to evaluate the surface roughness of pristine specimens. Further investigations on dislocation density were performed via electron channeling contrast imaging (ECCI) and the electron backscatter diffraction (EBSD) technique. These have been shown to be able to distinguish dislocation lines within about 10 nm separation.[62,63] For this purpose, an SEM (MIRA3 XMH, TESCAN, Brno, Czech Republic) equipped with a 4-quadrant BSE detector (DEBEN, Woolpit, UK) was employed. Later, the dislocation density was quantified by using the commercial software CrossCourt 4 (Acutance Scientific, Tunbridge Wells, UK) (Figure 3 and Figure S3).

2.5 | Microcontact electrochemical impedance spectroscopy

To access the local electrical response, microcontact-impedance spectroscopy was performed in the indentation-induced plastic zone and the regions away from it. For microcontact fabrication purposes, a thin layer (~150 nm) of $La_{0.6}Sr_{0.4}CoO_{3-\delta}$ (LSC) was deposited onto the specimens via pulsed laser deposition at 0.04 mbar O_2 background pressure and a substrate temperature of 600°C.[42] LSC was employed as an electrode material due to its high-temperature stability and large chemical capacitance, leading to a much better separation of electrode impedance and the response from bulk YSZ.[64,65] Further details on LSC target preparation are provided elsewhere.[66] Photolithography and chemical etching techniques[67] helped furbish microelectrodes (ME) in the desired regions, whereas fired Pt served as a

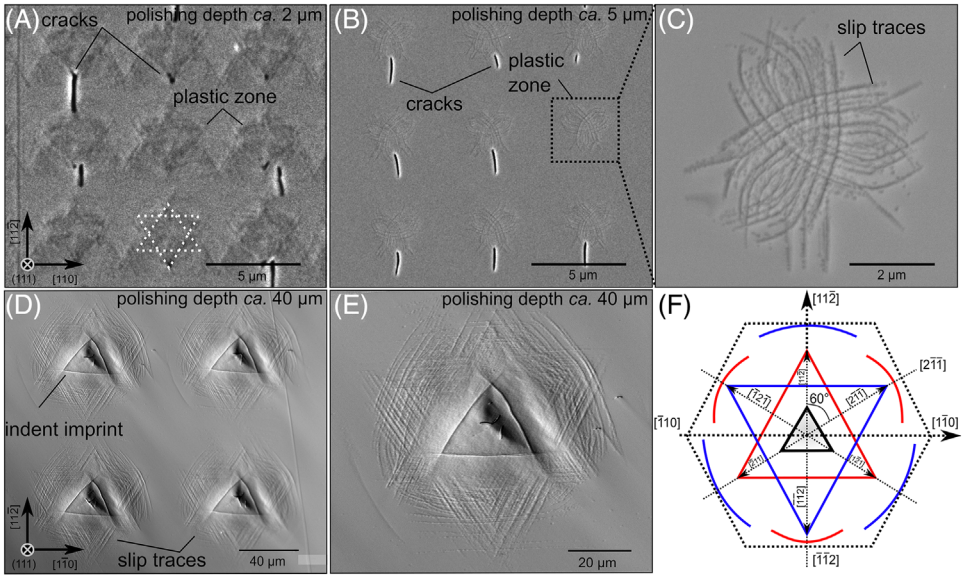

FIGURE 2 Indentation-induced mesoscopic dislocation structure: (A) field emission-scanning electron microscopy (FESEM) image of 3×3 array of Vickers indents shown in Figure 1B, at a polishing depth of ca. 2 μm, taken after chemical etching; (B) image of the same specimen in (a), now at a total polishing depth of ca. 5 μm and re-etching; (C) slip traces under a crack-free Vickers indent; (D) laser micrograph of a 4 N indent, created at 600°C substrate temperature, with a Berkovich pyramidal-shaped indenter on the same specimen as (A) taken after polishing down to ca. 40 μm and etching; (E) the plastic zone with the mesoscopic structure of dislocations is visualized via etch pit technique, imitating the "Star of David" pattern;[56] (F) dislocation etch-pits arrangement directions are sketched and labeled.

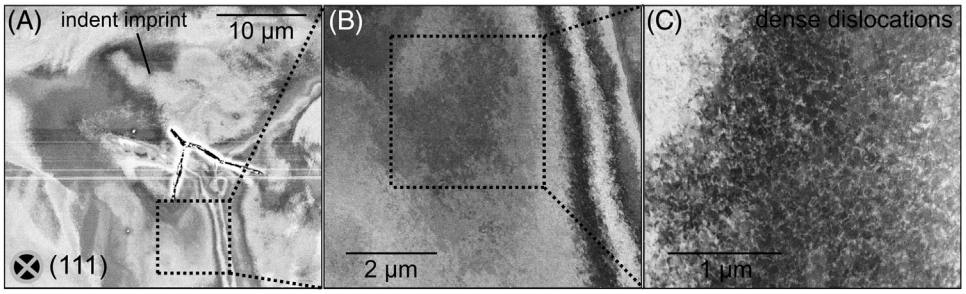

FIGURE 3 Electron channeling contrast imaging (ECCI) micrographs depicting mesoscopic dislocation density of specimen indented at a substrate temperature of 600°C, with Berkovich indenter: (A) a larger region is scanned next to the indentation imprint, accounting for the plastic zone; (B) narrowed down region, now focused within the plastic zone; (C) targeted ECCI micrograph depicting significantly higher dislocation density.

counter-electrode (CE) on the bottom for the specimens (Figure 4B,C). As chemical etching of LSC is prone to "over-etching" the structures, a photomask with 40 μm structures was used to obtain approx. 20 μm point contacts when optimizing the etching time. This was later confirmed with the help of an optical microscope (Figure S5). Sharp Pt–Ir needles were used to contact the ME inside an airtight chamber (Figure 4B,C). Electrical properties were investigated at 300°C via microcontact-impedance spectroscopy (Novocontrol Alpha-A Analyzer, Novocontrol, Montabaur, Germany) in the frequency range of 1 Hz–3 MHz with a voltage amplitude of 1 V.

3 | RESULTS AND DISCUSSION

3.1 | Room-temperature indentation and influence of dislocation slip on cracking

Room-temperature Vickers-indentation (with 0.1 N load) on YSZ (111) planes (Figure 1A,B) expectedly generated dislocations and activated two slip systems, with their respective Schmid factors (SF) of 0.47 for {001} ⟨110⟩ and 0.27 for {111} ⟨1 $\bar{1}$ 0⟩ slip system.[56] A SF of 0.5 implies the highest shear stress that can be applied on a slip plane in the slip direction; thus, optimum activation of the slip

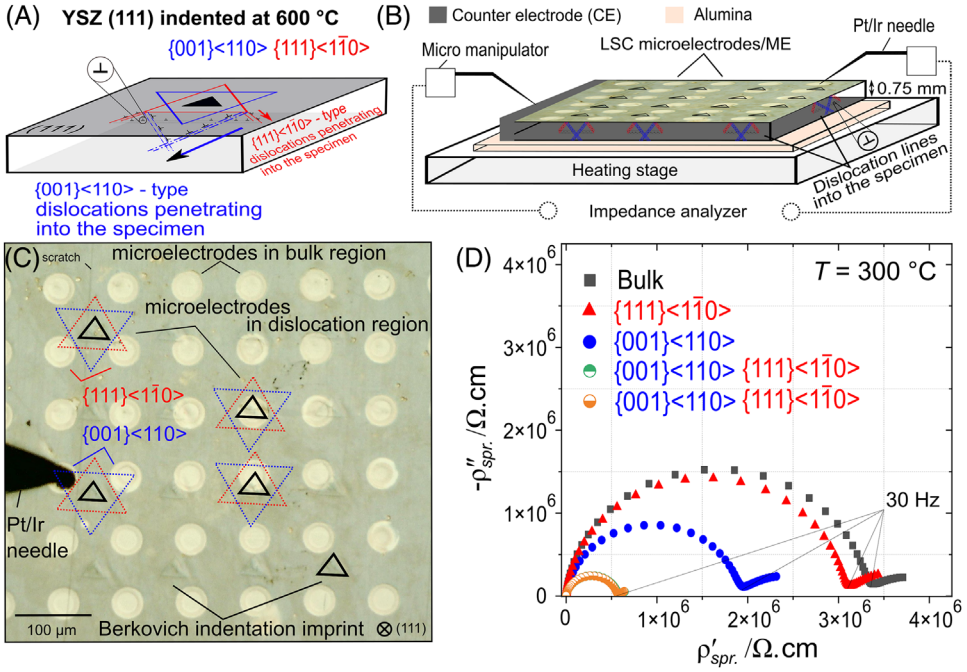

FIGURE 4 Indentation-induced slip traces and electrical analysis of pristine and dislocation regions: (A) schematic representing the slip traces when yttria-stabilized zirconia (YSZ) (111) planes are indented at high temperatures (e.g., 600°C); individual slip systems are traced, with dislocations percolating into the specimen (B) microcontacting setup illustration, depicting the YSZ specimen with an actual micrograph on top along with deposited LSC microcontacts; (C) top view of the same specimen; black triangles (Δ) highlighting the 4 × 4 array of Berkovich indentation imprints. Respective slip systems are traced with triangles (in red and blue), similar to Figure 2F. LSC microcontacts are furbished in a targeted manner onto the indentation-induced dislocation region and in bulk. Individual slip systems were electrically probed via sharp Pt/Ir microcontact needles; (D) Nyquist plot of electrical resistivity for representative electrodes measured at $T = 300$°C.

planes for plastic deformation can be reached.[52] Figure S2A strongly suggests the presence of dislocation arrays around the marked indents. However, performing indentation at room temperature also indicates the brittle fracture behavior in YSZ specimens, as severe cracking is observed on the indented surface (Figure S2A gives an enlarged view of Figure 1B). Both radial and lateral cracking can be seen with threefold radial crack symmetry along [11 $\bar{2}$] direction (highlighted in Figure S2A).[56] The cracking pattern symmetry can be understood by envisioning the interaction of dislocations. However, it is important first to comprehend the slip traces, potentially triggered by room-temperature indentation.[56]

Figure S2B features a cross-sectional schematic of the YSZ specimen; now, view from ⟨100⟩-direction, whereas the indents are marked on {111} planes.[56] This representation makes it possible to understand the threefold cracking symmetry observed for room-temperature indentation experiments (Figure S2A). First, the potentially activated slip systems, that is, {001} ⟨110⟩ and {111} ⟨1 $\bar{1}$ 0⟩ are traced at respective angles, with dislocations gliding on them. It is plausible that dislocations gliding on respective planes converge at {111} planes and form an immobile barrier (junction) that essentially acts as an obstruction against other dislocations moving in the plane.[68] This immobile barrier then results in crack formation normal to ⟨111⟩ directions.[56,68] For better illustration [111]-directions are sketched as dotted lines in Figure S2B (going from top to bottom). Using simple vector algebra, the cracking directions can now be rationalized, which are either [1 $\bar{1}$ 0] or [11 $\bar{2}$] directions. As both are perpendicular to [111], one of them can be visualized going into the plane of the paper/symbolized as ⊗.[56,68] The reason for these cracks is this immobile barrier of dislocations, also known as the Lomer–Cottrel junction or the Lomer lock. In literature, this phenomenon is reported as the "Cottrel mechanism".[6,69–72] Briefly, based on this mechanism, the threefold crack symmetry on {111} planes and the direction of crack traces can be understood. Additionally, this shows the importance of dislocation generation, their movement, and their interaction with the indentation-cracking properties of YSZ at room temperature.

3.2 | High-temperature indentation, plastic zones, and surface uplift

High-temperature indentation experiments were performed on YSZ (111) planes with the help of a Berkovich indenter (4 N load) at a substrate temperature of 600°C

(Figure 1C). For these experiments, cracking was successfully avoided. Instead, a material "pile-up" was observed around the indents, indicating high plastic flow in YSZ when indented at elevated temperatures (Figure 1C). This behavior was expected since dislocation glide becomes much easier at high temperatures with thermal activation.[57] A closer look at the regions around the indents revealed relatively large plastic zones (ca. 60 μm) with a hexagonal symmetry of slip traces (Figure 1C). This hints toward the existence of dense dislocation regions around and underneath the indents (further details follow in the next section).

3.3 | Indentation-induced mesoscopic dislocation structure

Figure 2 presents the indentation-induced mesoscopic dislocation structures on different length scales, including room (A–C) and high temperature (D–F) indented specimens. FESEM imaging (Figure 2A) of the specimen indented at room temperature (first polished down to 2 μm depth, followed by chemical etching) shows a plastic zone of ca. 5 μm in diameter; nevertheless, the cracks are still visible. Intuitively, the obtained plastic zone appears to be forming two opposite triangles (Figure 2A). This interesting feature can be associated with two slip systems activated based on the SF calculation while deforming YSZ in ⟨111⟩ direction.[73] More precisely, these slip systems are {001} ⟨110⟩ (SF 0.47) and {111} ⟨1 $\bar{1}$ 0⟩ (SF 0.27). Early studies on YSZ indentation suggest these slip systems are active only above 600°C.[56,57,68] However, no detailed description exists on the possibility of activating these slip systems at room temperature. This was presumably due to severe lateral and radial cracking, as presented in Figure S2A. As a result, limited attention was paid to the dislocation structures underneath the cracked surfaces. Nevertheless, our approach of sequential polishing of the indented (cracked) sample surfaces indicates that multiple slip systems can be activated even with indentation at room temperature. Regardless of the severe surface cracking, a controlled polishing rate, followed by chemical etching, reveals a plastic zone with dislocation clusters underneath (Figure 2A).

Serial polishing steps of the same specimen to an overall depth of ca. 5 μm removed the triangle-like slip traces (Figure 2A,B). However, the indentation-induced cracks are deemed grown enough, as they exist even at two–fold polishing depth. Nevertheless, another "lily flower"-like feature is observed at a polishing depth of ca. 5 μm (Figure 2B). Three individual bands of petals-like symmetry appear with a collective plastic zone size of <5 μm, which continues to the bottom of the plastic zone (Figure 2B,C). These petals of "lily flower"-like features are found to be tangent to [$\bar{1}$ 2 $\bar{1}$], [2 $\bar{1}$ $\bar{1}$], and [$\bar{1}$ $\bar{1}$ 2] set of directions (as highlighted in Figure 2F). However, at this polishing depth, that is, ca. 5 μm (Figure 2C), only the predominant {001} ⟨110⟩ slip system is likely to be active, as indicated in the literature.[57]

Even though room-temperature indentation reveals the activation of multiple slip systems with a strong interaction with each other (Figure 2A–C). The minuscule plastic zone (<5 μm) achieved after sequential polishing (to remove cracks) hinders the quantification of the mesoscopic dislocation structure. Moreover, such a localized region makes it hard to investigate any change in the functional properties potentially induced by dislocations. Therefore, further experiments were performed at a high-temperature indentation setup at 600°C. The images, taken before removing the indentation damage, already hint toward a relatively large plastic zone (ca. 60 μm) compared to the one at room temperature (Figure 1B,C). Additionally, the indentation was possible without causing cracks. A sequential polishing down to ca. 40 μm depth of the indented surface, followed by chemical etching of the obtained surface, revealed a 16 times larger plastic zone (now ca. 80 μm) compared to room-temperature indentation, that is, ca. 5 μm (comparing Figure 2A,D). Nevertheless, we note here that a load of 0.1 N was employed for indentation at room temperature (intended to minimize the cracking) but 4 N for high temperature. Therefore, an observed large plastic zone, in this case, should not be only associated with the indentation temperature but an increased load as well.

A more detailed investigation of the induced plastic zone exhibited three distinct features (Figure 2E). First, straight rows of dislocation etch pits parallel to the [1 $\bar{1}$ 0], forming a triangle with its vertices along [$\bar{1}$ 2 $\bar{1}$], [2 $\bar{1}$ $\bar{1}$], and [$\bar{1}$ $\bar{1}$ 2]. This is associated with the activated {001} ⟨110⟩ slip system with SF 0.47.[56] Second, for the relatively smaller triangle, the vertices' directions are found to be [11 $\bar{2}$], [1 $\bar{2}$ 1], and [$\bar{2}$ 11] and correspond to the {111} ⟨1 $\bar{1}$ 0⟩ slip system with SF 0.27.[56] Third, a hexagonal array around the indent is formed by rows of etch pits along the ⟨1 $\bar{1}$ 0⟩ and ⟨100⟩ corresponding to {111} and {100}, respectively.[56,57,68] These slip traces are featured schematically in Figure 2F; the two opposite triangles imitate a "Star of David," as observed earlier for room-temperature indentation as well (Figure 2A).[56]

Furthermore, a "curved" etch-pit configuration exists for both slip systems; refer to etch-pits in Figure 2E and the corresponding sketch in Figure 2F. The curved etch-pits are likely to be part of the triangles from the "Star of David" and hence related to the individual slip systems. However, the question arises on how the dislocation etch-pits align in a curved fashion. Holmes et al.,[57] described the reason being the different directions of the Burgers vector **b**. The curved etch-pit rows were associated to dislocation glide

on the, {001} ⟨110⟩ and {111} ⟨1 $\bar{1}$ 0⟩ slip systems, however, with Burgers vectors **b** inclined to the (111) surface.[57] The argument was further supported by Farber et al.,[68] which explains this phenomenon, considering the dislocation character in detail.[57,68]

It should be noted that the indenter geometry does not play a significant role in our experimental methodology; that is, in both cases (4-sided pyramid Vickers indenter at room temperature and 3-sided pyramid Berkovich indenter at 600°C), identical slip systems get activated (Figure 2A,D). However, in the latter case, the generated plastic zone and respective triangles were comparatively larger due to high load and higher dislocation mobility at elevated temperatures.[58]

3.4 | Mesoscopic dislocation density

Although an indentation-induced dense mesoscopic dislocation structure can be visualized in the form of etch pits around the indents (Figure 2D,E), a quantitative description of the dislocation density is difficult. This is because, inside the high-temperature indentation-induced plastic zone, the spacing between individual dislocations is so narrow that it can no longer be resolved by chemical etching (Figure 2E). To cope with this, ECCI was performed as with this technique dislocations can be imaged with a much larger field of view.[62] Systematic imaging was performed next to the indentation imprint accounting for the dislocation region (Figure 3A–C). A randomly distributed extremely dense dislocation structure with an overall dislocation spacing of ca. 50–70 nm was observed (Figure 3C), which leads to an average dislocation density of about 1×10^{14} m^{-2} within the scanned region. Given the technique's above-described limitations, the quantification is certainly correct within the order of magnitude, if not even better. Such a high-dislocation density within the plastic zone is realistic, as previously reported (ca. 3×10^{13} m^{-2}) in the bulk YSZ specimens, deformed at 1400°C.[50] Furthermore, in the current work, the deformation/indentation experiments are performed at relatively-low temperatures (600°C). Therefore, the low deformation temperature, in this case, also reduced the dislocation annihilation phenomenon, thus reducing the recovery of the dislocation structures and resulting in even higher dislocation density.[53,58]

Further information considering the dislocation density statistics was accessed using the EBSD technique, allowing lattice misorientation characterization in terms of mapping the geometrically necessary dislocations (GNDs).[63,74] This provides information on the dislocations remaining after unloading and being responsible for the local misorientations. Therefore, a semiquantitative analysis is feasible for these structural units (dislocations) on a larger scale to better evaluate the indentation-enhanced dislocation density. Figure S3 provides EBSD maps of bulk and dislocation-rich areas, depicting each region's GNDs density. A significant difference is observed by comparing the pristine GNDs (ca. 4×10^{11} m^{-2}) to the GNDs inside the plastic zone (ca. 2×10^{14} m^{-2}). To estimate an "exact dislocation density," evaluation of the Nye tensor is plausible[75,76]; however, this is beyond the scope of this work, as EBSD data supports the ECCI results and is in excellent agreement with the images obtained via chemical etching (Figure 2D,E). We also note that the EBSD analysis was performed on an unetched specimen after fine polishing with a surface roughness <30 nm. Therefore, any artifacts potentially introduced by polishing damage or chemical etching were omitted.

3.5 | Local electrical investigations (microcontact electrochemical impedance spectroscopy)

The electrical response of indentation-induced mesoscopic dislocation structures was investigated using microcontact electrochemical impedance spectroscopy for the specimens with large plastic zones/indented at 600°C. This technique allows quantifying the local electrical response, as most of the applied voltage is expected to drop just under the probed microcontact.[60] In this case, the electrical resistivity (ρ) could be estimated in terms of the spreading resistivity $\rho_{spr.} = 2dR$, assuming a homogeneous resistance in the probed region.[60,77,78] However, this is still rather a qualitative investigation, as we do not have a fully homogeneous phase with constant resistivity below the ME.[60,79] This means that the measured resistance depends on the density and the extent of the dislocation network below the electrode. The large back surface was used as the CE. Figure 4A presents the cross-sectional schematic, illustrating the activated slip traces when YSZ (111) planes were indented with a Berkovich indenter (similar to Figure 2F) and further models the dislocation arrangement on respective slip planes.[56] Both slip systems, that is, {001} ⟨110⟩ (blue) and {111} ⟨1 $\bar{1}$ 0⟩ (red), are sketched at respective angles with (111) planes to demonstrate the dislocation propagation into the specimen. With this configuration, the dislocation lines are likely to percolate into the specimen, as shown in a pseudo-3D schematic of the specimen in Figure 4B. The same specimen is now portrayed in Figure 4C, with LSC ME furbished onto and between the dislocation-rich regions, which are later probed with Pt/Ir needles (Figure 4C). It should be noted that indentation imprints are still discernible, and this helps locate the plastic zone, earlier found to be at least ca. 80 μm

(Figure 2D,E). Taking this into account, the so-called "Star of David" is traced around the indent imprints for better visualization. The large plastic zone around the indent and the minuscule ME of 20 μm allowed for measuring the apparent electrical response of the individual slip systems (Figure 4C).

Nyquist plots of spreading electrical resistivity ($\rho_{spr.}$) were measured at $T = 300°C$ for the pristine (bulk) and indentation-enhanced dislocation regions on the same specimen and provided in Figure 4D. When measuring the bulk region, a single semicircle was recorded (data points in black), along with a serial electrode arc at lower frequencies in the range of 30–1 Hz. The data was found to be imitating a depressed semicircle and, therefore, was fitted using an equivalent circuit consisting of a resistance (R) with a constant phase element (CPE) in parallel (i.e., $R \parallel CPE$).[80] Later, the true capacitance "C" value was extracted from "CPE," which was found to be 2×10^{-12} F. This capacitance indicates that the corresponding resistance reflects a bulk property and not an electrode process.[81] There exists a difference in the electrical response when measuring the microcontacts located onto the {111} ⟨1 $\bar{1}$ 0⟩ slip system or sketched (red) triangle, pointing upward (Figures 2F and 4C). A decrease in the $\rho_{spr.}$ is realized when compared to the bulk data (black and red curves in Figure 4D). A further decrease in the $\rho_{spr.}$ is recorded when measuring on the {001} ⟨110⟩ slip system or triangles marked in blue, pointing downward (Figures 2F and 4C). Remarkably, the trend of reduction in the resistivity is even more prominent in the collective impedance response of these slip systems (comparing black to orange/green curves in Figure 4D).

The difference between the electrical resistivity of the bulk region and the {111} ⟨1 $\bar{1}$ 0⟩ slip system may be misleading, as this is still in the range of the error bar. However, a significant change in the resistivity is induced by the {001} ⟨110⟩ slip system compared to the bulk, which remains below a factor of 2. Nevertheless, a substantial decrease in the resistivity can be observed in the regions where both {001} ⟨110⟩ and {111} ⟨1 $\bar{1}$ 0⟩ slip systems are supposedly operating. It should be noted that this is a similar region scanned by ECCI in Figure 3A–C, depicting an extremely dense mesoscopic dislocation structure. Therefore, these differences in electrical resistivity evolve from higher dislocation density. In other words, the dense dislocation networks under the indents enhanced the local electrical conductivity by many factors. The exact magnitude of enhancement, however, remains elusive because quantification requires a homogeneous material below the ME. To ensure reproducibility, at least two microcontacts were measured in the respective regions, with Figure 4D presenting the representative data.

Besides, it is worth discussing the role of individual slip systems in the observed electrical conductivity enhancement. For example, one may argue that if the dislocation density is the only responsible parameter, then why do the individual slip systems show a different electrical response? Furthermore, the dislocation penetration depth into the specimen remains unclear so far, as Figure 4A,B only provides a schematic of the slip systems percolating into the specimen. To address this, we consider the results by Heuer et al.,[56–58] where indentation-induced dislocation structures in ~9YSZ are investigated in detail. The side-view of post-indentation and etched {100} planes revealed a remarkably high dislocation density, with an experimental indication that the predominant {001} ⟨110⟩ slip system penetrates deeper compared to {111} ⟨1 $\bar{1}$ 0⟩ slip systems.[56] The difference in the penetration depth of these two slip systems[56] thus should explain the observed different electrical responses (Figure 4D). In other words, the {111} ⟨1 $\bar{1}$ 0⟩ slip system percolates to a shorter depth below the ME, which only leads to a minor impact on measured conductivity. On the other hand, the {001} ⟨110⟩-type slip system penetrates the specimens comparatively deeper, which extends the highly conductive region below the electrode. Moreover, in the areas where these two slip systems, that is, {111} ⟨1 $\bar{1}$ 0⟩ and {001} ⟨110⟩ interact with a multiplied dislocation density, a substantial increase in electrical conductivity is conceivable. Remarkably, this conductivity enhancement is above what can be achieved by point defect engineering in 9YSZ. If this could solely be attributed to oxygen diffusion, this outclasses the solubility limits of YSZ concerning the point defect doping and renders dislocations a powerful tool to engineer electrical conductivity. In previous work, we at least found evidence for high oxygen transport in dislocation-rich regions produced by activating the secondary ⟨110⟩ {110}, ⟨111⟩ {110} slip systems.[50] However, no actual diffusion or incorporation coefficient could be obtained because the diffusion profile at the dislocation extended deep into the sample and could not be fully resolved. This means that we cannot attribute the higher electrical transport to oxygen diffusion at this point. There is, nevertheless, certainly a contribution from higher oxygen incorporation or diffusion due to the presence of dislocations. Moreover, just because dislocations from these two slip systems allow for higher oxygen transport, it does not automatically mean that the {001} ⟨110⟩ slip system induces high oxygen conductivity. As mentioned, the electrical properties can be very different depending on the slip system, dislocation type (edge, screw, or mixed), and dislocation core structure.[28,30] The induced dislocations are never straight for YSZ and show looping, kinks, and jogs. Thus, the character of the dislocations changes significantly even within the same slip plane. This counts for any slip system.[44,45] As a result, the dominant mobile charge carrier could even change along a single dislocation. Nevertheless, given the previous computational data

and experimental evidence, oxygen transport is highly likely to dominate electrical transport.[49,50] Electromotive force measurements with deformed YSZ will be necessary to ultimately prove this and are currently prepared.

A broader application of dislocation–tuned conductivity concept calls for developing methodologies to produce even larger plastic zones. To this end, we suggest marking indents closer to each other in a way that their plastic zone overlap or performing cyclic indentation in the same region to enhance the dislocation density further, as recently reported by Okafor et al.[82] Nevertheless, special attention needs to be paid to experimental details, as overlapping plastic zones or cyclic loading may induce severe work hardening and result in cracking, especially in the case of ceramic electrolytes. Further design parameters would include thinning the rear side of the specimen, as it is hypothesized that if dislocations percolate all the way through, an even higher electrical conductivity can be achieved.[29] Indeed, there are ample opportunities to tailor the dislocation structures in ceramics and tune their electrical conductivity by mechanical deformation.

4 | CONCLUSIONS

In summary, we demonstrate a significant increase in the electrical conductivity of 9YSZ by mechanically induced dislocations at the mesoscale. Employing the micromechanical approach well below the dislocation recovery temperature helped generate extremely dense dislocation structures. This reduced dislocation annihilation and allowed tailoring of the dislocation structures much more effortlessly compared to bulk deformation. This technique also helped the individual analysis of activated slip systems, which is impossible in bulk deformed specimens. The control over mesoscopic dislocation structures revealed the potential of dislocations to enhance the electrical conductivity in ceramic electrolytes even higher than achieved by chemical doping strategies. Nevertheless, the final proof of high oxygen conductivity being the only reason for the higher electrical transport in YSZ is still required.

ACKNOWLEDGMENTS

The authors are grateful to Prof. Dr. -Ing. Jürgen Rödel (Technical University of Darmstadt, Germany) for the helpful discussions. Qaisar Khushi Muhammad acknowledges the Deutscher Akademischer Austauschdienst (DAAD) for the fellowship with award number 91669061. Xufei Fang thanks the Athene Young Investigator program at TU Darmstadt. Kuan Ding (https://orcid.org/0000-0003-0633-1954) is acknowledged for his contributions to performing AFM measurements. Many thanks to Martin Krammer (https://orcid.org/0000-0003-4352-4800) and Tobias Huber (https://orcid.org/0000-0001-6339-8341) (TU Wien, Austria) for supporting the LSC microelectrode deposition. Matthäus Siebenhofer was supported by the K1-COMET center CEST (Centre for Electrochemical Surface Technology, Wiener Neustadt), funded by the Austrian Research Promotion Agency (FFG) (award number 865864) and by the Austrian Science Fund (FWF) (project number P31654-N37). Open access funding enabled and organized by Projekt DEAL.

Open access funding enabled and organized by Projekt DEAL.

ORCID

Qaisar Khushi Muhammad https://orcid.org/0000-0002-6976-7651
Xufei Fang https://orcid.org/0000-0002-3887-0111
Till Frömling https://orcid.org/0000-0002-8827-1926

REFERENCES

1. Eshelby JD. Dislocations as a cause of mechanical damping in metals. Proc R Soc Lond, A. 1949;197(1050):396–416.
2. Mott N. The mechanical properties of metals. Proc Phys Soc Sect B. 2002;64:729–41.
3. Broudy R. Dislocations and mechanical properties of crystals. J Am Chem Soc. 1958;80(18):5009–10.
4. Pavlov V. Effect of screw dislocations on mechanical properties of metals with bcc lattice. Fiz Met Metalloved. 1978;45(4):815–37.
5. Pelleg J. Mechanical properties of ceramics. Cham: Springer Science & Business Media; 2014.
6. Hull D, Bacon DJ. Introduction to dislocations. Oxford: Elsevier; 2011.
7. Wachtman Jr J, Maxwell I. Plastic deformation of ceramic-oxide single crystals. J Am Ceram Soc. 1954;37(7):291–99.
8. Wachtman Jr J, Maxwell L. Plastic deformation of ceramic-oxide single crystals, II. J Am Ceram Soc. 1957;40(11):377–85.
9. Ashbee KHG, Smallman RE. The plastic deformation of titanium dioxide single crystals. Proc R Soc Lond A. 1963;274(1357):195–205.
10. Ashbee K, Smallman R. Stress-strain behavior of titanium dioxide (rutile) single crystals. J Am Ceram Soc. 1963;46(5):211–14.
11. Phillips Jr W. Deformation and fracture processes in calcium fluoride single crystals. J Am Ceram Soc. 1961;44(10):499–506.
12. Evans AG, Pratt P. Dislocations in the fluorite structure. Philos Mag. 1969;20(168):1213–37.
13. Argon A, Orowan E. Plastic deformation in MgO single crystals. Philos Mag. 1964;9(102):1003–21.
14. Copley SM, Pask JA. Plastic deformation of MgO single crystals up to 1600°C. J Am Ceram Soc. 1965;48(3):139–46.
15. Gilman J, Johnston WG, Sears G. Dislocation etch pit formation in lithium fluoride. J Appl Phys. 1958;29(5):747–54.
16. Johnston W, Gilman J. Dislocation multiplication in lithium fluoride crystals. J Appl Phys. 1960;31(4):632–43.
17. Gilman J, Johnston W. Dislocations in lithium fluoride crystals. Solid State Phys. 1962;13:147–222.

18. Karch J, Birringer R, Gleiter H. Ceramics ductile at low temperature. Nature. 1987;330(6148):556–58.
19. Dokko PC, Pask JA. Plastic deformation of ceramic materials. Mater Sci Eng. 1976;25:77–86.
20. Fries E, Guiberteau F, Dominguez-Rodriguez A, Cheong D-S, Heuer A. High-temperature plastic deformation of Y_2O_3-stabilized ZrO_2 single crystals. I. The origin of the yield drop and associated glide polygonization. Philos Mag A. 1989;60:107–21.
21. Cheong D-S, Dominguez-Rodriguez A, Heuer AH. High-temperature plastic deformation of Y_2O_3-stabilized ZrO_2 single crystals. II. Electron microscopy studies of dislocation substructures. Philos Mag A. 1989;60:123–38.
22. Cheong D-S, Rodriguez AD, Heuer AH. High-temperature plastic deformation of Y_2O_3-stabilized ZrO_2 single crystals III. Variation in work hardening between 1200 and 1500°C. Philos Mag A. 1991;63(3):377–88.
23. Dominguez-Rodriguez A, Cheong D-S, Heuer AH. High-temperature plastic deformation in Y_2O_3-stabilized ZrO_2 single crystals: IV. The secondary slip systems. Philos Mag A. 1991;64:923–9.
24. Heuer AH. Transformation toughening in ZrO_2-containing ceramics. J Am Ceram Soc. 1987;70:689–98.
25. Bravo-León A, Jiménez-Melendo M, Domínguez-Rodríguez A. Mechanical and microstructural aspects of the high temperature plastic deformation of yttria-stabilized zirconia polycrystals. Acta Metall Mater. 1992;40:2717–26.
26. Dominguez-Rodriguez A, Jiménez-Melendo M, Castaing J. Plasticity of zirconia. In: Plastic deformation of ceramics. New York: Springer; 1995. p. 31–41.
27. Adepalli KK, Kelsch M, Merkle R, Maier J. Influence of line defects on the electrical properties of single crystal TiO_2. Adv Funct Mater. 2013;23:1798–806.
28. Muhammad QK, Porz L, Nakamura A, Matsunaga K, Rohnke M, Janek J, et al. Donor and acceptor-like self-doping by mechanically induced dislocations in bulk TiO_2. Nano Energy. 2021;85:105944–53.
29. Muhammad QK, Bishara H, Porz L, Dietz C, Ghidelli M, Dehm G, et al. Dislocation-mediated electronic conductivity in rutile. Mater Today Nano. 2022;17:100171.
30. Porz L, Frömling T, Nakamura A, Li N, Maruyama R, Matsunaga K, et al. Conceptual framework for dislocation-modified conductivity in oxide ceramics deconvoluting mesoscopic structure, core, and space charge exemplified for $SrTiO_3$. ACS Nano. 2020;15:9355–67.
31. Etsell T, Flengas SN. Electrical properties of solid oxide electrolytes. Chem Rev. 1970;70(3):339–76.
32. Nakamura A, Wagner JB. Defect structure, ionic conductivity, and diffusion in yttria stabilized zirconia and related oxide electrolytes with fluorite structure. J Electrochem Soc. 1986;133(8):1542–8.
33. Mahato N, Banerjee A, Gupta A, Omar S, Balani K. Progress in material selection for solid oxide fuel cell technology: a review. Prog Mater Sci. 2015;72:141–337.
34. Kendall K, Kendall M. High-temperature solid oxide fuel cells for the 21st century: fundamentals, design and applications. Amsterdam: Elsevier; 2015.
35. Arachi Y, Sakai H, Yamamoto O, Takeda Y, Imanishai N. Electrical conductivity of the ZrO_2–Ln_2O_3 (Ln = lanthanides) system. Solid State Ionics. 1999;121:133–39.
36. Knauth P, Tuller HL. Solid-state ionics: roots, status, and future prospects. J Am Ceram Soc. 2002;85:1654–80.
37. Kumar B, Chen C, Varanasi C, Fellner JP. Electrical properties of heterogeneously doped yttria stabilized zirconia. J Power Sources. 2005;140(1):12–20.
38. Hui SR, Roller J, Yick S, Zhang X, Decès-Petit C, Xie Y, et al. A brief review of the ionic conductivity enhancement for selected oxide electrolytes. J Power Sources. 2007;172(2):493–502.
39. Haering C, Roosen A, Schichl H. Degradation of the electrical conductivity in stabilised zirconia systems: Part I: Yttria-stabilised zirconia. Solid State Ionics. 2005;176(3):253–9.
40. Haering C, Roosen A, Schichl H, Schnöller M. Degradation of the electrical conductivity in stabilised zirconia system: Part II: Scandia-stabilised zirconia. Solid State Ionics. 2005;176(3–4):261–68.
41. Koettgen J, Grieshammer S, Hein P, Grope BOH, Nakayama M, Martin M. Understanding the ionic conductivity maximum in doped ceria: trapping and blocking. Phys Chem Chem Phys. 2018;20:14291–321.
42. Ahamer C, Opitz A, Rupp G, Fleig J. Revisiting the temperature dependent ionic conductivity of yttria-stabilized zirconia (YSZ). J Electrochem Soc. 2017;164:F790–803.
43. Zakaria Z, Abu Hassan SH, Shaari N, Yahaya AZ, Boon Kar Y. A review on recent status and challenges of yttria stabilized zirconia modification to lowering the temperature of solid oxide fuel cells operation. Int J Energy Res. 2020;44(2):631–50.
44. Otsuka K, Kuwabara A, Nakamura A, Yamamoto T, Matsunaga K, Ikuhara Y. Dislocation-enhanced ionic conductivity of yttria-stabilized zirconia. Appl Phys Lett. 2003;82(6):877–9.
45. Otsuka K, Matsunaga K, Nakamura A, Ii S, Kuwabara A, Yamamoto T, et al. Effects of dislocations on the oxygen ionic conduction in yttria stabilized zirconia. Mater Trans. 2004;45(7):2042–7.
46. Kushima A, Yildiz B. Oxygen ion diffusivity in strained yttria stabilized zirconia: where is the fastest strain? J Mater Chem. 2010;20(23):4809–19.
47. Hojo H, Tochigi E, Mizoguchi T, Ohta H, Shibata N, Feng B, et al. Atomic structure and strain field of threading dislocations in CeO_2 thin films on yttria-stabilized ZrO_2. Appl Phys Lett. 2011;98(15):153104.
48. Yildiz B. Stretching the energy landscape of oxides—effects on electrocatalysis and diffusion. MRS Bull. 2014;39:147–56.
49. Feng B, Ishikawa R, Kumamoto A, Shibata N, Ikuhara Y. Atomic scale origin of enhanced ionic conductivity at crystal defects. Nano Lett. 2019;19(3):2162–8.
50. Muhammad QK, Scherer M, Opitz AK, Taibl S, Boehme C, Rohnke M, et al. Dislocation-mediated oxygen–ionic conductivity in yttria-stabilized zirconia. ACS Nano. 2022;16(10):16655–67.
51. Messerschmidt U, Baufeld B, Baither D. Plastic deformation of cubic zirconia single crystals. Key Eng Mater. 1998;153:143–82.
52. Messerschmidt U. Dislocation dynamics during plastic deformation. Berlin-Heidelberg: Springer-Verlag; 2010.
53. Pelleg J. Creep in ceramics. Cham: Springer Science & Business Media; 2017.
54. Stich S, Ding K, Muhammad QK, Porz L, Minnert C, Rheinheimer W, et al. Room-temperature dislocation plasticity in $SrTiO_3$ tuned by defect chemistry. J Am Ceram Soc. 2021;105(2):1–12.

55. Fang X, Bishara H, Ding K, Tsybenko H, Porz L, Höfling M, et al. Nanoindentation pop-in in oxides at room temperature: dislocation activation or crack formation? J Am Ceram Soc. 2021;104(9):4728–41.
56. Morscher GN, Pirouz P, Heuer AH. Temperature dependence of hardness in yttria-stabilized zirconia single crystals. J Am Ceram Soc. 1991;74(3):491–500.
57. Holmes D, Heuer A, Pirouz P. Dislocation structures around Vickers indents in 9.4 mol% Y_2O_3-stabilized cubic ZrO_2 single crystals. Philos Mag A. 1993;67(2):325–42.
58. Farber BY, Chiarelli A, Heuer A. Dislocation velocities in cubic zirconia (ZrO_2) single crystals. Philos Mag A. 1995;72(1):59–80.
59. Minnert C, Oliver WC, Durst K. New ultra-high temperature nanoindentation system for operating at up to 1100°C. Mater Des. 2020;192:108727.
60. Fleig J. Microelectrodes in solid state ionics. Solid State Ionics. 2003;161(3–4):279–89.
61. Meyerhoff R, Bailey D, Smith J. X-ray diffraction camera for the alignment of large single crystals. Rev Sci Instrum. 1961;32(6):715–17.
62. Crimp MA. Scanning electron microscopy imaging of dislocations in bulk materials, using electron channeling contrast. Microsc Res Tech. 2006;69(5):374–81.
63. Wilkinson AJ, Britton TB. Strains, planes, and EBSD in materials science. Mater Today. 2012;15(9):366–76.
64. Rupp GM, Schmid A, Nenning A, Fleig J. The superior properties of $La_{0.6}Ba_{0.4}CoO_{3-\delta}$ thin film electrodes for oxygen exchange in comparison to $La_{0.6}Sr_{0.4}CoO_{3-\delta}$. J Electrochem Soc. 2016;163(6):F564.
65. Siebenhofer M, Huber TM, Friedbacher G, Artner W, Fleig J, Kubicek M. Oxygen exchange kinetics and nonstoichiometry of pristine $La_{0.6}Sr_{0.4}CoO_{3-\delta}$ thin films unaltered by degradation. J Mater Chem A. 2020;8(16):7968–79.
66. Opitz AK, Rameshan C, Kubicek M, Rupp GM, Nenning A, Götsch T, et al. The chemical evolution of the $La_{0.6}Sr_{0.4}CoO_{3-\delta}$ surface under SOFC operating conditions and its implications for electrochemical oxygen exchange activity. Top Catal. 2018;61(20):2129–41.
67. Taibl S, Fafilek G, Fleig J. Impedance spectra of Fe-doped $SrTiO_3$ thin films upon bias voltage: inductive loops as a trace of ion motion. Nanoscale. 2016;8(29):13954–66.
68. Farber BY, Chiarelli A, Heuer A. A dislocation mechanism of crack nucleation in cubic zirconia single crystals. Philos Mag A. 1994;70(1):201–17.
69. Cottrell AH. Theory of brittle fracture in steel and similar metals. Trans Metall Soc AIME. 1958;212(2):192–203.
70. Rodriguez P. Sixty years of dislocations. Bull Mater Sci. 1996;19(6):857–72.
71. Hirth JP, Lothe J, Mura T. Theory of dislocations. J Appl Mech. 1983;50(2):476.
72. Anderson PM, Hirth JP, Lothe J. Theory of dislocations. Cambridge: Cambridge University Press; 2017.
73. Schmid E, Boas W. Kristallplastizität: mit Besonderer Berücksichtigung der Metalle (Crystal plasticity: with special attention to metals). Berlin-Heidelberg: Springer-Verlag; 2013.
74. Wilkinson AJ, Britton TB, Jiang J, Karamched PS. A review of advances and challenges in EBSD strain mapping. IOP Conf Ser: Mater Sci Eng. 2014;55:012020.
75. Pantleon W. Resolving the geometrically necessary dislocation content by conventional electron backscattering diffraction. Scr Mater. 2008;58(11):994–7.
76. Wheeler J, Mariani E, Piazolo S, Prior D, Trimby P, Drury M. The weighted Burgers vector: a new quantity for constraining dislocation densities and types using electron backscatter diffraction on 2D sections through crystalline materials. J Microsc. 2009;233(3):482–94.
77. Fleig J, Maier J. Point contacts in solid state ionics: finite element calculations and local conductivity measurements. Solid State Ionics. 1996;86:1351–6.
78. Fleig J, Rodewald S, Maier J. Microcontact impedance measurements of individual highly resistive grain boundaries: general aspects and application to acceptor-doped $SrTiO_3$. J Appl Phys. 2000;87(5):2372–81.
79. Bishara H, Tsybenko H, Nandy S, Muhammad QK, Frömling T, Fang X, et al. Dislocation-enhanced electrical conductivity in rutile TiO_2 accessed by room-temperature nanoindentation. Scr Mater. 2022;212:114543–7.
80. Lvovich VF. Impedance spectroscopy: applications to electrochemical and dielectric phenomena. Hoboken, NJ: John Wiley & Sons; 2012.
81. Macdonald JR, Johnson WB. Fundamentals of impedance spectroscopy. Hoboken, NJ: John Wiley & Sons; 2018.
82. Okafor C, Ding K, Zhou X, Durst K, Rödel J, Fang X. Mechanical tailoring of dislocation densities in $SrTiO_3$ at room temperature. J Am Ceram Soc. 2022;105(4):2399–402.

SUPPORTING INFORMATION

Additional supporting information can be found online in the Supporting Information section at the end of this article.

How to cite this article: Muhammad QK, Valderrama M, Yue M, Opitz AK, Taibl S, Siebenhofer M, et al. Dislocation-tuned electrical conductivity in solid electrolytes (9YSZ): A micro-mechanical approach. J Am Ceram Soc. 2023;106:6705–6716.
https://doi.org/10.1111/jace.19291